Optimal design of polymer-based microneedle for improved collection of whole blood from human fingers

Hoa Le Thanh, Hai Le The, Vy Nguyen, Nhut Tran-Minh, Kaiying Wang, Frank Karlsen

Department of Micro and Nano Systems Technology (IMST), Buskerud and Vestfold University College, Postboks 235, 3603 Kongsberg, Norway
E-mail: thanhhoa.hcmut@gmail.com

Published in Micro & Nano Letters; Received on 11th May 2014; Revised on 4th August 2014; Accepted on 5th August 2014

A highly applicable theoretical model and a simple, inexpensive mould-based method is introduced to design and fabricate the pyramid-shaped SU-8 microneedle. The main purpose is to be able to extract blood at point-of-care sites from up to 80% of typical nurse-home patients with a disorder of blood circulation in fingers and toes (Raynaud's phenomenon). Geometry optimisation was conducted based on the study of fracture force, which can be accurately predicted by the proposed theoretical model. The accuracy of the proposed theoretical model was confirmed by the finite element study and practical measurement. For practical verification, measurement of fracture force was conducted on fabricated SU-8 microneedles, including a 1470 μm-tall pyramid-shaped microneedle and a 1515 μm-tall traditional-shaped microneedle. The measurement results confirmed the improved strength of the proposed pyramid-shaped microneedle, especially of the pyramidal tips, which can exhibit significantly higher applied force with 2.82 N compared with the 0.51 N bevel tip. Practical tests of skin penetrability on human fingers showed that the microneedles fabricated with the proposed geometry may be sharp and strong enough to safely puncture human skin and long enough to reach the blood vessels.

1. Introduction: Early diagnostic and pre-disease detection are extremely important to increase patient survival rates. Accuracy and reliability are highly desirable for the adequate selection of suitable therapeutics. The aim of the POCNAD project has been to develop a platform for the rapid screening or diagnosis of clinical or environmental variations that is a related-gene activity. The platform is desired to operate with seven main functions of patient sample collection, concentration/separation, pre-treatment, preparation, purification, amplification and target detection. For the blood-sampling device, hypodermic needles are traditionally utilised in every healthcare system for direct blood collection from veins. However, because of a number of downsides, such as insertion pain, tissue trauma [1], patient discomfort or needle phobia [2], lack of convenience and user-friendly ability [3], the requirement of expertise and specialised medical knowledge for implementation [4], the utilisation of hypodermic needles has been replaced by a new approach of sample collection related (SCR) microscale needles, that is, microneedles. This is especially for patients who need periodic and continuous monitoring, for example, diabetic patients [5]. The first main purpose of SCR microneedle arrays is to make human blood available in any health station, nursing home or family home. The second main purpose is to make it possible to extract blood from a typical point-of-care setting including patients or old people with very low blood circulation. The main challenge for health personnel, relating to low blood circulation or a disordered blood circulation (Raynaud's phenomenon) or reduced systolic pressures in the fingers, is that of using conventional needles to remove any whole blood sample.

During the practical implementation of microneedles, the breaking of the microneedle, particularly tip fracture, is one of the most crucial issues. The broken part may remain inside the human skin or enter the blood vessels, causing injury, inflammation or abrasion. Therefore, geometry optimisation is highly desirable, especially with a blood-sampling microneedle (the length must be longer than 1500 μm [6]). One frequently used approach is to minimise the failure possibility to ensure as high a safety level as possible. Previously, a number of studies on mechanical failure have been conducted with either mathematical or simulation models [7–10]. The failure criteria of yield strength and shear strength may provide better accuracy for the prediction of fracture force [11].

With regard to the manufacturing of microneedles, many studies on metallic microneedles have been reported, for example, titanium microneedles [12] and nickel microneedles [13]. Although metallic microneedles typically have good biocompatibility and mechanical properties, the manufacture process is normally expensive and time consuming [14]. Moreover, pre-constructed moulds are required for metal deposition [6, 13, 15]. On the other hand, polymer-based microneedles can be fabricated using conventional UV lithography, thus reducing significantly the fabrication costs and allowing fabrication of complex structures. In our research, SU-8 was selected because of its following advantages: (i) SU-8 is a photo-reactive polymer (i.e. photon-induced polymerisation), allowing the construction of complex three-dimensional (3D) high-aspect-ratio structures, (ii) its good mechanical properties [16] and (iii) its reported biocompatibility [17, 18]. In addition, the biocompability of the fabricated SU-8 microneedles can be improved with surface modifications, for example, deposition of biocompatible metals, for example, titanium, platinum or nickel.

In this Letter, we propose a stronger design of pyramid-shaped microneedles (PMNs) that may exhibit safer skin penetration. The improved mechanical strength of the PMNs was verified by comparison of fracture force with traditional-shaped microneedles (TMNs). Then, the geometry optimisation was conducted based on the proposed PMN. The accuracy and reliability of the fracture analysis of the proposed pyramid-shaped hollow microneedles were verified by the finite element method with COMSOL and practical measurements. To fabricate high-aspect-ratio hollow microneedles, we utilised the mould-based method in [19]. According to this method, conventional SU-8 lithography and PDMS micromoulds are combined to develop a low-cost, simple method with good repeatability and high throughput. The skin penetrability of our proposed pyramid-shaped hollow microneedle was also tested by inserting a single/array of PMN into human fingers to evaluate the practical performance of the fabricated PMNs from many aspects, such as mechanical failures, skin penetrability and extraction ability.

© The Institution of Engineering and Technology 2014

doi: 10.1049/mnl.2014.0242

2. Geometry optimisation by structural analysis: PMNs are expected to improve the mechanical performance (i.e. larger force endurance) with the special features of the square base, off-centre lumen and pyramidal tip. The structural strength of PMNs was studied through the investigation of fracture forces, including critical buckling load (P_{cr}) and maximum bending force (P_b). The dimension of each geometrical feature can also be optimised with the study on fracture forces.

2.1. Analytical and numerical solutions: The first failure mechanism to be considered is structural buckling. To calculate critical buckling load (P_{cr}), (1) was utilised. This formula has been used in a number of studies to compute P_{cr} of various cross-section structures, such as tapered hollow microneedles [8] and square pyramid columns [11]. In our previous work [20], this approach was applied particularly for PMNs. In the work reported in this Letter, (1) was utilised to estimate P_{cr} of two different designs of microneedles such as PMNs and TMNs:

$$P_{cr} = \frac{E\pi^2}{2L^3}\int_0^L \sum_{i=0}^{n} I(z).\cos^2\left(\frac{\pi z}{2L}\right)\mathrm{d}z \tag{1}$$

The second failure mechanism is because of the transverse force, that is, bending force. Typically, bending force is most likely to induce fracture at the microneedle shaft subjected to the largest bending moment. However, microneedle tips are considerably breakable because of the diminutive tip size (~40 µm). The possibility of tip failure may be subsequently higher than that of shaft failure. In this work, we developed a theoretical model to compute the magnitude of shear stress when the microneedle is subjected to a distributed bending force. With higher applicability to various structural designs, this model may predict more accurately the fracture bending force. As illustrated in Fig. 1*a*, the equation of stress balance in the *x*-direction is presented in (2):

$$\int_A \sigma \mathrm{d}A + \tau_{yx}A_{xy} = \int_{A+\mathrm{d}A} (\sigma + \mathrm{d}\sigma)\mathrm{d}A \tag{2}$$

$$\Rightarrow \int_A \sigma \mathrm{d}A + \tau_{yx}D(x,y)\mathrm{d}x = \int_{A+\mathrm{d}A} (\sigma + \mathrm{d}\sigma)\mathrm{d}A \tag{3}$$

$$\Rightarrow \left(\frac{M(x)}{I_z(x)} + d\left(\frac{M(x)}{I_z(x)}\right)\right)\int_{A+\mathrm{d}A} y\mathrm{d}A - \frac{M(x)}{I_z(x)}\int_A y\mathrm{d}A = \tau_{yx}D(x,y)\mathrm{d}x \tag{4}$$

The integrals in (4) are observed to be the expression for the first moment of area $Q_z(x, y)$. Consequently, (4) becomes

$$\Rightarrow \left(\frac{M(x)}{I_z(x)} + d\left(\frac{M(x)}{I_z(x)}\right)\right)(Q_z - \mathrm{d}Q_z) - \frac{M(x)}{I_z(x)}Q_z = \tau_{yx}D(x,y)\mathrm{d}x \tag{5}$$

Equation (5) can be simplified by neglecting high-order components. Thus, the final expression of shear stress (τ_{xy}) can be deduced as follows:

$$\tau_{xy} = \tau_{yx} = \frac{1}{D(x,y)}\left(\frac{M(x)}{I_z(x)}\frac{\mathrm{d}Q_z}{\mathrm{d}x} + Q_z\frac{\mathrm{d}}{\mathrm{d}x}\left(\frac{M(x)}{I_z(x)}\right)\right) \tag{6}$$

where $D(x, y)$ is the applying width of shear stress, $Q_z(x, y)$ and $I_z(x)$ are the first and second moments of area and $M(x)$ is the bending moment resulting from the distributed bending force P_b. All components are illustrated in Fig. 1*b*.

For PMNs, the components in (6) were computed for five different cross-sectional areas corresponding to five regions of *x*. The

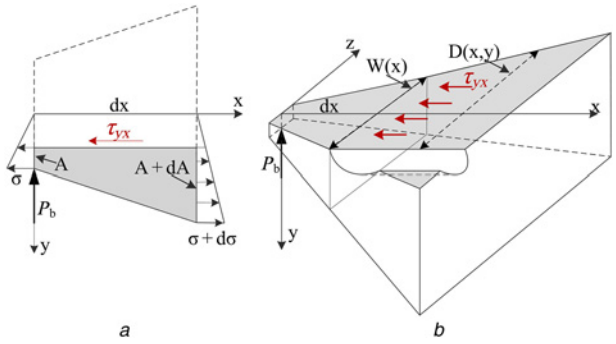

Figure 1 *Illustrations for shear stress derivation. σ and σ + dσ are normal stress distributed on the area A and A + dA. τ_{yx} is assumed to be uniform in the z-direction. P_b represents the distributed bending force acting on the y-direction*
a Stress balance in the *xOy* plane
b Distribution of shear stress (τ_{yx}) in pyramidal tip

calculations were conducted by programming with Maple software. The theoretical results were then verified by the COMSOL simulator under the same boundary conditions. Specifically, the whole structural parameters were variable except that the bottom is set to be a fixed constraint. A distributed force $P_b = 0.105$ N is applied on the shaded area in Fig. 2*a* with $X_0 = 152$ µm. The values of shear stress can be extracted from the stress tensor. Distribution of τ_{xy} is presented in *x*–*y* coordinates, and it is assumed to be uniform in the *z*-direction and symmetrical on the *y*-axis.

2.2. Analytical analysis results and numerical simulation results: Fig. 2 shows the matching of shear stress between the analysis and simulation results. There are two critical points, the first MAX (global maximum at X_0) and the second MAX (local maximum at the diminutive edge) (see Fig. 2), at which fracture is most likely to happen. Good matching between the analysis and simulation results can be observed in Figs. 2 and 3. The standard deviation is about 6.5 and 25.4% for the first and second MAX point, respectively. Since the concentrated stress is distributed in a diminutive edge at the second MAX point, the magnitude of τ_{yx} is significantly increased. In practice, the fabricated microneedle will not exhibit this problem because the fabrication of extremely sharp features is very challenging in practice. However, the prediction of τ_{yx} at the second MAX helps to verify the accuracy of our proposed model. Fig. 3*b* depicts how τ_{yx} at the first MAX point reduces with an increase in X_0.

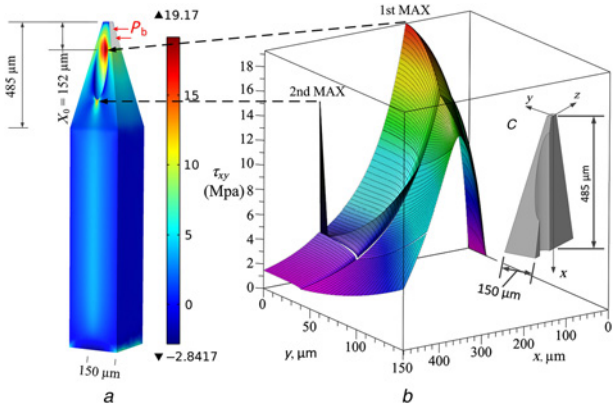

Figure 2 *Distribution of shear stress (τ_{xy}) at the microneedle tip when P_b is applied in the shaded area (X_0 = 152 µm)*
a 3D distribution from simulation results
b 3D distribution from theoretical calculation
c Illustration for system coordinates on a half of pyramidal tip

© The Institution of Engineering and Technology 2014

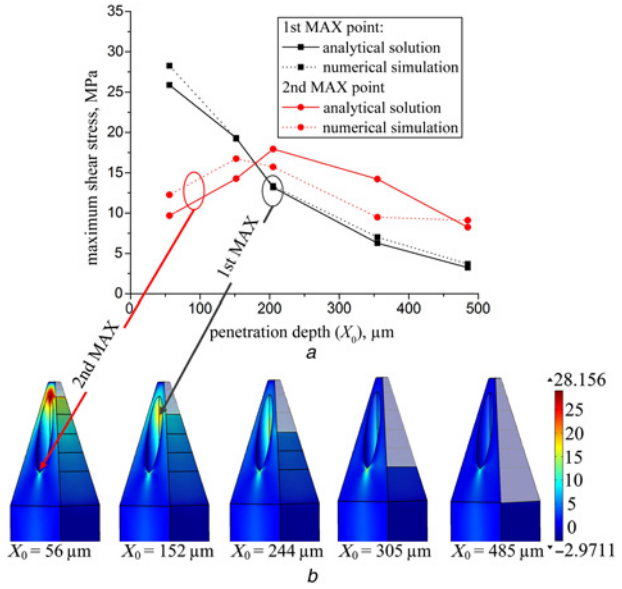

Figure 3 *Matching of the results from simulation and calculation results*
a 2D plot of the matching of τ_{xy} magnitude at the first and second MAX point
b 3D distribution of τ_{xy} from simulation with X_0: 56–485 μm

Moreover, the tip failure is most likely to occur before shaft failure. By comparing $(\tau_{yx})_{max}$ to the shear strength of SU-8 (19.5 MPa), P_b can be deduced.

The relationship between P_{cr} and the base width (W_1) was investigated with W_1 ranges from 200 to 400 μm. The effect of length (L) was also taken into account with two values of L: 1800 and 1500 μm. The results are shown in Fig. 4. The endurance of the PMNs against axial force is about 1.7 times higher than that of the TMNs, verifying the improved strength of the PMNs. In Fig. 4*b*, we can see that the possibility of a tip breaking is significantly high when $X_0 = 152$ μm (i.e. the puncturing point of a microneedle into human skin). When $W_1 = 300$ μm and $L = 1500$ μm, the proposed PMNs can withstand 2.94 N (axial force) and 0.105 N (bending force at $X_0 = 152$ μm) compared with 1.71 N (axial force) and 0.065 N (bending force at $X_0 = 152$ μm) of the TMNs. The theoretical results show that the pyramidal tip may be stronger than the bevel tip in terms of bending force resistance.

With the same procedure as presented, this model can be applied for other structures, such as TMNs, the tapered-tip microneedle or the truncated cone microneedle, for a more accurate prediction of fracture bending force.

3. Fabrication of microneedles: To develop an inexpensive method with high throughput for the fabrication of a microneedle,

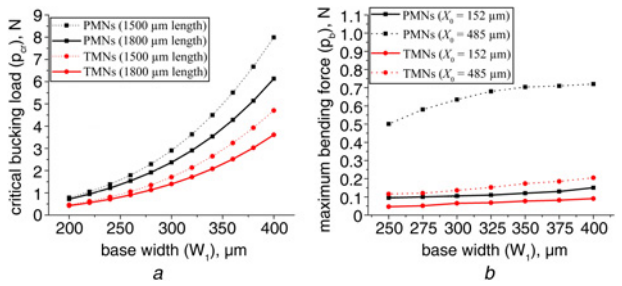

Figure 4 *Results from mathematical frameworks. The analysis was applied for MNs with 300 μm in base width, 120 μm in hollow diameter and 40 μm in tip radii*
a Critical buckling load (P_{cr}) against base width (W_1)
b Maximum bending force (P_b) against base width (W_1)

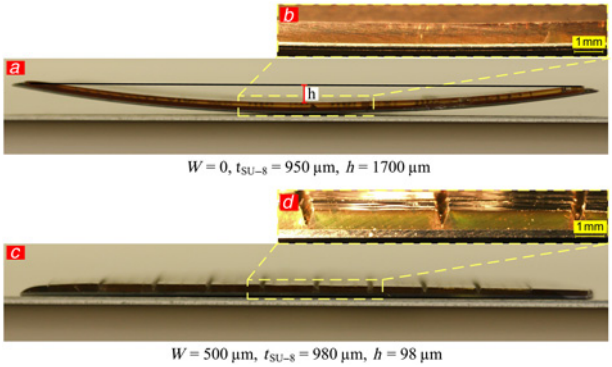

Figure 5 *Illustration for the advantage of separated lines*
a and *b* 950 μm-thick SU-8 layer, $W = 0$, $h = 1700$ μm
c and *d* 980 μm-thick SU-8 layer, $W = 500$ μm, $h = 98$ μm

two mould-based methods with SU-8 epoxy photoresist (MicroChem, Newton, MA) were proposed and compared (see Fig. 6). Figs. 6*a* and *b* present the procedure to construct the pyramidal tips by using 4-times inclined exposure. The top part is relatively rotated 90° at each time of exposure. The actual tip angle will be reduced because of the effect of light refraction ($n_{air} = 1$ and $n_{SU-8} = 1.668$ [21]). Therefore, a tip angle of 25° is achievable with a 35°-angle aluminium holder. Fig. 6*c* presents the concept of two fabrication methods, including method 1 (moulding of microneedles) and method 2 (direct formation of microneedles). The difference between two methods is at steps 2–4 in Fig. 6*c*. At step 1 in Fig. 6*c*, SU-8 coating was performed using the weight-controlled method, that is, the thickness of the coated layer is controlled by weighing SU-8 2150 ($\rho = 1.19$ kg/m^3) before pouring onto the substrate. 600 μm-thick and 1100 μm-thick SU-8 layers are achievable with 3.3 g and 5.8 g SU-8 2150, respectively. The sample was soft-baked for 15 min at 65°C and 4 h at 95°C followed by 4-times inclined exposure with an exposure dosage of 700 mJ/cm^2 for each time of exposing. The 500 μm-tall pyramidal tips were obtained after 10 minutes development. With the process on the silicon wafer, wafer bending is a serious issue, which subsequently may lead to misalignment, poor adhesion and cracks. We proposed a solution, named 'separated line', to reduce the effect of internal stress in multilayer structures of thick SU-8 film, which subsequently may cause wafer bending [22]. Separated lines were patterned on a photomask to separate and reduce the stress applying area (see Figs. 5*c* and d), thus providing more space for SU-8 to expand/compress upon heating/cooling. The optimal width of the separated line (W) was numerically and experimentally studied to be 500 μm. A test on a 3-inch silicon wafer was conducted to examine the advantage of the separated line. The wafer bending reduced significantly from 1700 μm (see Fig. 5*a*) to 98 μm (see Fig. 5*c*) for the cases without separated lines and with 500 μm-wide separated lines, respectively.

Method 2 is first considered. At step 2.2, a primary PMDS mould with pyramidal tips was constructed by performing inverse moulding two times. A 1000 μm-thick SU-8 layer was then coated on the PDMS mould. The sample was soft-baked for 15 min at 65°C and 10 h at 95°C. A double exposure step was then conducted with an exposure dosage of 3000 and 300 mJ/cm^2 to form the microneedle shaft and the support plate, respectively. The hollow microneedle array was obtained after 30 minutes development with ultrasonic agitation followed by gentle separation. On the other hand, in method 1, after the pyramidal tips were constructed, a master mould of microneedle-shaped holes was obtained after exposure (step 2.1). The primary PDMS mould was created by performing inverse PDMS moulding twice (see step 3.1 in Fig. 6*c*).

Our experiments indicate that method 2 is relatively better than method 1 in terms of the quality of fabricated microneedle tips,

© The Institution of Engineering and Technology 2014

doi: 10.1049/mnl.2014.0242

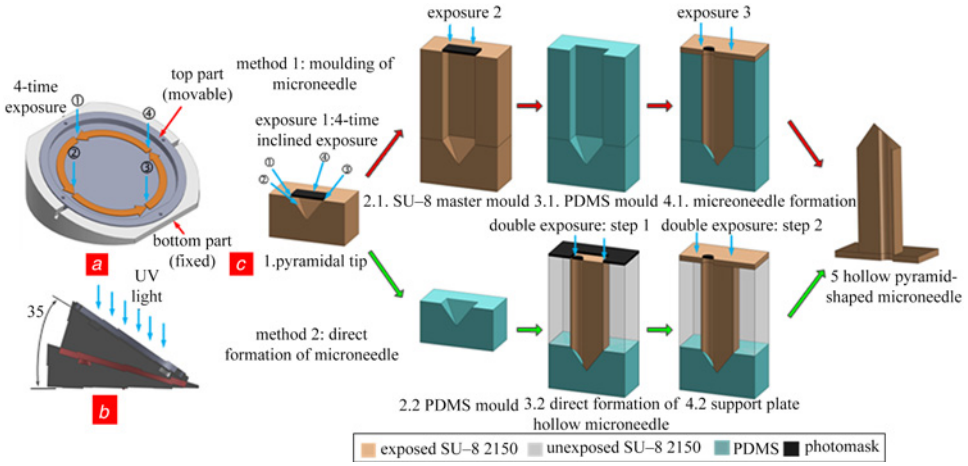

Figure 6 *Illustrations for fabrication of polymer-based hollow microneedles*
a Principle of the inclined exposure
The top part is movable and can be rotated 90° relative to the bottom part
The sample was exposed four times to form the pyramidal structure
b Illustration for the inclined exposure with the aluminium holder
c Process flow of two methods for the fabrication of microneedles, the Figures are shown in cross-sectional view

repeatability, fabrication time and cost. At step 3.1 in Fig. 6*c*, when performing PDMS moulding/unmoulding, the high-aspect-ratio structures were easily broken, and subsequently led to the imperfection or destruction of the final moulded microneedles. In addition, the possibility of successfully fabricating microneedle hollows in method 2 is higher than that of method 1. The effect of light scattering is a more critical at step 4.1 in Fig. 6*c* because of the large opening area (150 µm diameter of the patterned feature). In method 2, microneedle separation is easier.

For the fabrication of TMNs, we utilised method 2. The bevel tip was created on a 25° sloped wall. The microneedle shaft, hollow and the support plate were formed by double exposure. TMNs were obtained after SU-8 development and separation. PMNs were fabricated with a 1470 µm total length (490 µm tip and 980 µm shaft), 310 µm base width, 43 µm tip radii and a 210–330 µm-thick support plate. TMNs were fabricated with a 1515 µm total length (627 µm tip and 888 µm shaft), 314 µm base width, 39 µm tip radii and 200 µm-thick support plate (see Fig. 7). Compared with the designed hollow diameter of 120 µm, the measured hollow diameter is 115 and 116 µm for PMNs and TMNs, respectively. Scattering of UV light might result in the reduction of the hollow diameter.

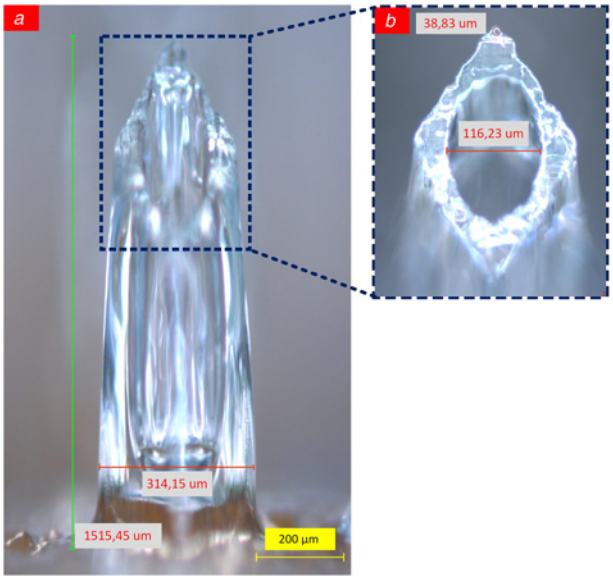

Figure 7 *Optical micrograph of microfabricated TMN which was measured to be 1515 µm in length, 314 µm in length, 116 µm in hollow diameter and 39 µm in tip radii*
a Side-view of one TMN
b Bevelled tip of TMN

4. Performance evaluation

4.1. Measurement of fracture force: The measurement setup on the Shear Tester Delvotec 5600 is shown in Fig. 8. The microneedle is mounted on the force driving tip. The movement is precisely controlled by a built-in motor with a resolution of 0.01 N. To measure the fracture force, a rigid surface (1 mm-thick aluminium plate with 10 GPa in Young's modulus) was used as a penetration object. To minimise the effect of slipperiness, a thin layer of epoxy resin UN3082 was spun on an aluminium plate. This layer provides a softer surface to immobilise the microneedle tip. Thus, the measurement error because of the slippery surface can be minimised. The measurements were conducted repeatedly three times each for the PMNs and TMNs.

The force–time plot was recorded and displayed on the screen as shown in Fig. 9. The failure point was determined automatically by the system when there is a sudden decrease of applied force. There are two points at which the microneedles were broken,

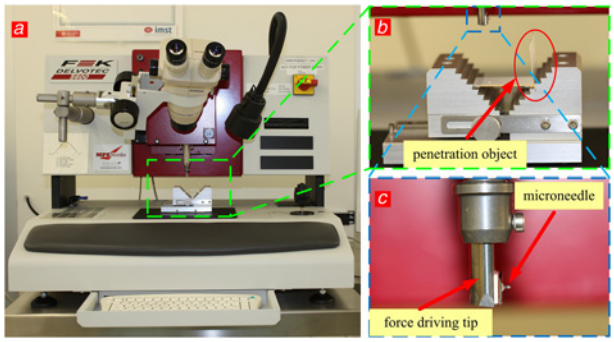

Figure 8 *Photograph of testing instrument for the measurement of fracture force*
a Equipment setup on Shear Tester Delvotec 5600
b Microneedle and penetration object (aluminium plate)
c Microneedle is mounted on the force driving tip

© The Institution of Engineering and Technology 2014

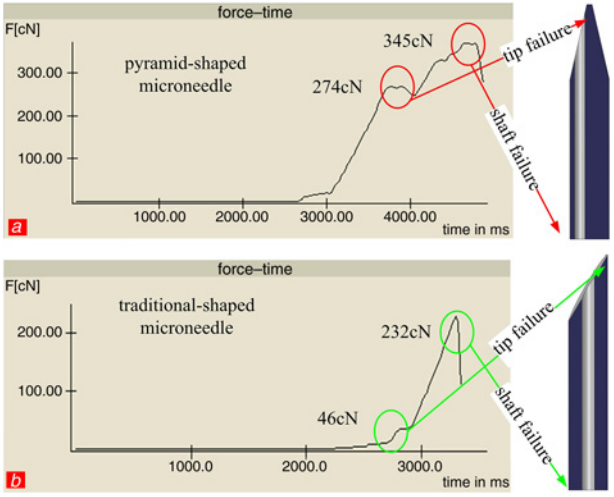

Figure 9 *Measurement results of fracture force of PMNs and TMNs. The forces were recorded against applying time*
a Force–time measurement plot of PMNs
b Force–time measurement plot of TMNs

Table 1 Measurements of fracture axial force were performed on PMNs (1470 μm in length, 310 μm in base width, 115 μm in hollow diameter) and TMNs (1515 μm in length, 314 μm in base width, 116 μm in hollow diameter)

Type of MNs	Measured force, N				Calculated force (shaft failure), N	Difference (shaft failure), %
	Shaft failure	$\bar{\sigma}$, %	Tip failure	$\bar{\sigma}$, %		
PMNs	3.4	1.8	2.82	2.0	3.2	8.16
TMNs	2.37	2.1	0.51	7.8	1.71	29.5

corresponding to tip failure and shaft failure. PMNs exhibited higher fracture forces (2.74N for tip failure and 3.45N for shaft failure) compared with TMNs (0.46N for tip failure and 2.32N for shaft failure).

The average measured forces are presented in Table 1. Comparison with the results from the theoretical study, the average differences are 8.16% and 29.5% for the PMNs and TMNs, respectively. When the microneedle tip is broken, the total length is reduced. Fracture force thus increased. With an average tip-fracture force of 2.82N, the pyramidal tip may be stronger than the bevel tip which only can withstand a maximum force of 0.51N.

4.2. Skin penetrability: Skin penetrability of the fabricated microneedles was assessed on volunteers' fingers, as shown in Fig. 10. Two scenarios were conducted on human fingers for a single microneedle and a 3 × 3 SU-8 microneedle array. After the sterilisation process, the microneedles were pressed perpendicularly against the human finger by manually pushing them and then pulled out by metallic tweezers. The insertion process was optically inspected under a Olympus MVX10 microscope as depicted in Fig. 10.

In scenario 1, the single PMNs were safely inserted into human skin. The fabricated microneedles were shown to be able to penetrate the skin barrier without breaking. Tip breaking was not observed when separating the microneedles from the human finger. Figs. 10*a* and *b* show an inserted PMN and the insertion spot at which the presence of blood was observed. In scenario 2, an array of PMNs has successfully punctured the human finger. According to the testing results, the fabricated PMNs (42 × 42 μm

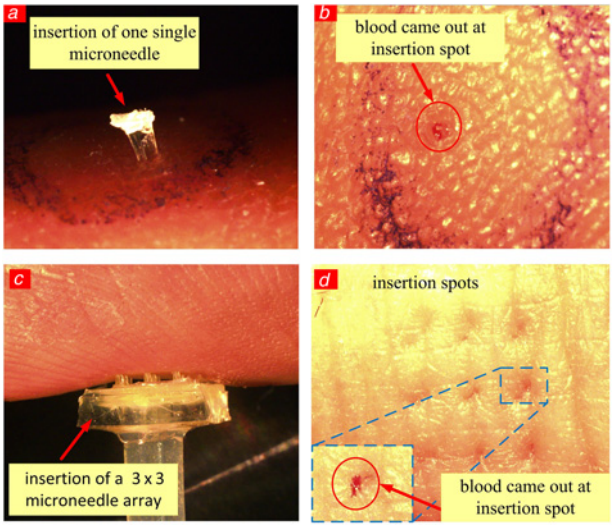

Figure 10 *Skin penetrability was tested on volunteer's finger with one single PMN and a 3 × 3 array of PMNs. After insertion, insertion spots can be inspected on the volunteer's finger*
a Inserted single PMNs into human finger
b Insertion spot of single PMNs on human finger
c Inserted PMNs array into human finger
d Insertion spot of 3 × 3 array of PMNs on human finger

tip) were able to be inserted safely into human skin with the configuration of the microneedle array. Specifically, it is easier to perform vertical insertion on a 3 × 3 array than a single microneedle. Moreover, the pre-positioned microneedles on the array made it possible for vertical insertion. The array fabricated with 1500 and 2000 μm microneedle pitch was experimentally proved to be potentially penetrable into human skin compared with the array with the 1200 μm pitch. To avoid breaking of the support plate, the thickness of the support plate can be controlled by adjusting the exposure dosage at step 4.2 in Fig. 6*c*. The optimal thickness was experimentally chosen to be thicker than 300 μm. Figs. 10*c* and *d* illustrate a successful skin penetration of the fabricated microneedles array with a 330 μm-thick support plate (300 mJ/cm^2).

After separation of a single microneedle and an array of microneedles, at the insertion spots, as depicted by red circles in Figs. 10*b* and *d*, blood came out and there was blood at the microneedle tips. The appearance of blood indicates that the fabricated microneedles were able to puncture the skin and reach the blood vessels. Blood did not flow through the needle lumens and it seemed to stop at the microneedle tips. One possible explanation is that the suction pressure (i.e. negative pressure) generated by an external pump may be required for extraction. Several pumping systems have been reported, for example, a piezoelectric microactuator [10] or a syringe pump (New Era Pump Systems, USA) [6]. The aim of this experiment was to test the skin penetrability and this was achieved, giving the preliminary results for the further development of a functional prototype of microneedle-based blood-sampling devices.

5. Conclusion: This Letter proposes an optimal design of PMNs for whole blood collection. The geometry of the proposed microneedle is optimised to minimise the possibility of breaking. A mathematical model is introduced to predict the facture bending force based on shear strength criterion with the verifications of simulation and measurement on fracture force. The proposed method of the direct formation of microneedles was experimentally shown to be potentially feasible for mass production. In addition, the concept of method 2 opens a new path to develop an inexpensive method that is suitable for mass production. For future development, we suggest constructing an aluminium-based sample with the proposed

© The Institution of Engineering and Technology 2014

doi: 10.1049/mnl.2014.0242

structures (i.e. sloped walls and pyramidal trenches) in this Letter for a replacement of micromachined structures, which can be formed by using KOH-etching of silicon (pyramidal trenches or V-groove structures) or inclined UV lithography. In a forthcoming paper, a simple, low-cost manufacturing method combined by CNC machining technology and UV lithography will be presented. Furthermore, an adequate testing protocol is necessary for more accurate biological evidence. Further testing has to be done to prove whether these microneedles are more useful for the collection of whole blood from fingers with reduced systolic blood pressure.

6. Acknowledgments: This work was conducted at the Buskerud and Vestfold University College with support from the two companies Norchip and ORP.

7 References

[1] McAllister D.V., Allen M.G., Prausnitz M.R.: 'Microfabricated microneedles for gene and drug delivery', *Ann. Rev. Biomed. Eng.*, 2002, **2**, (1), pp. 289–313

[2] Hamilton J.G.: 'Needle phobia: a neglected diagnosis', *J. Fam. Pract.*, 1995, **41**, (2), pp. 169–175

[3] Prausnitz M.R.: 'Analysis: overcoming skin's barrier: the search for effective and user-friendly drug delivery', *Diabetes Technol. Ther.*, 2001, **3**, (2), pp. 233–236

[4] Zhang P., Dalton C., Jullien G.A.: 'Design and fabrication of MEMS-based microneedle arrays for medical applications', *Microsyst. Technol.*, 2009, **15**, (7), pp. 1073–1082

[5] Mukerjee E., Collins S., Isseroff R., Smith R.: 'Microneedle array for transdermal biological fluid extraction and in situ analysis', *Sens. Actuators A, Phys.*, 2004, **114**, (2), pp. 267–275

[6] Li C.G., Lee C.Y., Lee K., Jung H.: 'An optimized hollow microneedle for minimally invasive blood extraction', *Biomed. Microdevices*, 2013, **15**, (1), pp. 17–25

[7] Kuo S.C., Chou Y.: 'A novel polymer microneedle arrays and PDMS micromolding', *Tamkang J. Sci. Eng.*, 2004, **7**, pp. 95–98

[8] Kim K., Park D.S., Lu H.M., Che W., Kim K., Lee J.B., Ahn C.H.: 'A tapered hollow metallic microneedle array using backside exposure of SU-8', *J. Micromech. Microengineering*, 2004, **14**, (4), pp. 597–603

[9] Zahn J., Talbot N., Liepmann D., Pisano A.: 'Microfabricated polysilicon microneedles for minimally invasive biomedical devices', *Biomedical Microdevices*, 2000, **2**, pp. 295–303

[10] Tsuchiya K., Nakanishi N., Nakamachi E.: 'Development of blood extraction system designed by female mosquito's blood sampling mechanism for bio-MEMS', *Biomed. Appl. Micro and Nanoeng.*, 2005, **5651**, pp. 379–388

[11] Ji J., Tay F.E., Miao J., Iliescu C.: 'Microfabricated microneedle with porous tip for drug delivery', *J. Micromech. Microeng.*, 2006, **16**, (5), pp. 958

[12] Tsuchiya K., Nakanishi N., Uetsuji Y., Nakamachi E.: 'Development of blood extraction system for health monitoring system', *Biomed. Microdevices*, 2005, **7**, (4), pp. 347–353

[13] Kim K., Park D.S., Lu H.M., Che W., Kim K., Lee J.B., Ahn C.H.: 'A tapered hollow metallic microneedle array using backside exposure of SU-8', *J. Micromech. Microeng.*, 2004, **14**, (4), p. 597

[14] Chaudhri B.P., Ceyssens F., De Moor P., Van Hoof C., Puers R.: 'A high aspect ratio SU-8 fabrication technique for hollow microneedles for transdermal drug delivery and blood extraction', *J. Micromech. Microeng.*, 2010, **20**, (6), p. 064006

[15] Davis S.P., Martanto W., Allen M.G., Prausnitz M.R.: 'Hollow metal microneedles for insulin delivery to diabetic rats', *IEEE Trans. Biomed. Eng.*, 2005, **52**, (5), pp. 909–915

[16] Lorenz H., Despont M., Fahrni N., LaBianca N., Renaud P., Vettiger P. : 'SU-8: a low-cost negative resist for MEMS', *J. Micromech. Microeng.*, 1997, **7**, (3), p. 121

[17] Voskerician G., Shive M.S., Shawgo R.S., Recum H.V., Anderson J. M., Cima M.J., Langer R.: 'Biocompatibility and biofouling of MEMS drug delivery devices', *Biomaterials*, 2003, **24**, (11), pp. 1959–1967

[18] Cho S.H., Lu H.M., Cauller L., Romero-Ortega M.I., Lee J.B., Hughes G.A. : 'Biocompatible SU-8-based microprobes for recording neural spike signals from regenerated peripheral nerve fibers', *IEEE Sens. J.*, 2008, **8**, (11), pp. 1830–1836

[19] Luttge R., Berenschot E.J., de Boer M.J., Altpeter D.M., Vrouwe E.X., van den Berg A., Elwenspoek M.: 'Integrated lithographic molding for microneedle-based devices', *J. Microelectromech. Syst.*, 2007, **16**, (4), pp. 872–884.

[20] Le-Thanh H., Tran-Minh N., The H.L., Karlsen F.: 'A novel design of hollow microneedle for blood extraction'. Proc. IEEE Int. Conf. on Nano/Micro Engineered and Molecular Systems, Hyatt Regency Waikiki Beach Resort and Spa, Hawaii, USA, 2014, pp. 430–435

[21] Mitra S.K., Chakraborty S.: 'Microfluidics and nanofluidics handbook: fabrication, implementation, and applications' (CRC Press, 2011), vol. 2

[22] Li B., Liu M., Chen Q.: 'Low-stress ultra-thick SU-8 UV photolithography process for MEMS', *J. Micro/Nanolithography MEMS MOEMS*, 2005, **4**, (4), pp. 043008–043008

© The Institution of Engineering and Technology 2014